Three-dimensional annular saturated crack propagation in ultralow permeability rock under wave & electro-magneto-thermo-elastic fields

BoJing Zhu[1,2*],YaoLin Shi[1] ,TianYou Fan[3]

[1] Key Laboratory of Computational Geodynamics of CAS, University of Chinese Academy of Sciences, Beijing 100049, CHINA

[2] Rock Mechanics Laboratory, University of Durham, Durham DH1 3LE, UK

[3] Beijing Institute of Technology, Beijing 100081,CHINA

* Corresponding author: cynosureorion@ucas.ac.cn (B.J.Zhu)

Abstract: This contribution presents a new theory with lattice Boltzmann & finite element & hypersingular integral equation (LB-FE-HIE) to explore the three-dimensional pore-network cracks transient hydrofacturing-liquefaction in tight sandstone (3D PC-TH-TS) under seismic waves & electro-magneto-thermo-elastic fields through intricate theoretical analysis and numerical simulations. First, the 3D PN-TH-TS problem is reduced to solving a set of coupled LB-FE-HIEs by using the Green functions and distribution functions, in which the unknown functions are the extended pore-network cracks displacement discontinuities. Then, the behavior of the extended displacement discontinuities at the pore-network cracks surface terminating at the solid-liquid film interface are analyzed through extended dynamic hypersingular integral main-part analysis method of LB-FE-HIEs. Closed formed solutions for the extended singular dynamic stress, the extended dynamic stress intensity factor and the extended dynamic energy release rate near the dislocations interface are provided. Last, the tight sandstone sample from the Ordos Basin Triassic formation is selected, the fluid-solid coupled digital rock physical modeling is established, and the simulations of 3D PC-TH-TS process is presented on the parallel CPU-GPU platform. The hydrofacturing-liquefaction varying with the amplitude, frequency and constituting time of earthquake wave is obtained. The relationship between the tight sandstone pore-network cracks transient propagation-evolution and the maximum tight sandstone fracturing-liquefaction stress criteria is explored.

Keywords Hydrofracturing-liquefaction, tight sandstone, lattice Boltzmann method, finite element method, hypersingular integral equation, seismic wave & electro-magneto-thermo-elastic fields, parallel CPU-GPU technology.

1. Introduction

Hydrofracturing-liquefaction mechanism is the basic theory for understanding the in-situ stress measurement, the petroleum-gas (nature gas and shale gas)-geothermic develop, and the earthquake evaluation and mechanism exploration. With the complex and challenge of this issue, the mechanism of dynamic Hydrofracturing-liquefaction is still not clear even a lot of fundamental and landmark achievements have been obtained in this field since the last century 60's. The oscillation singularity of dynamic stress wave as well as stress oscillation singularity index of pore-network cracks transient Hydrofracturing-liquefaction (PC-TH) fluid pore-solid sketch interface under seismic wave & electro-magneto-thermo-elastic fields (SW&EMTE) makes it much more difficult than the unsaturated cased of the ordinary cracks, for in this process, including fluid transient undrained process, fluid transient compression and expansion process, physical properties of tight

stone varying with PC-TH propagation process and tight stone transient failure with the liquefaction process (the liquefaction process time is around 10E-5s).

The mode I stress intensity factor for a constant velocity semi-infinite crack moving in a fluid-saturated porous medium with finite height is calculate[1]. The linear elastic solid with cavities containing nonviscous compressible fluid is explored[2], and the abnormally high fluid pressure in the cavities affects is analyzed. The mode I crack in an elastic fluid-saturated porous solids is studied[3], and relatively closed-form asymptotic solution near the crack tip is obtained. Extended horizontal cracks in a vertical column of saturated sand is explored [4], and the theory is good qualitative agreement with the experimental findings. The interaction of a normally incident time-harmonic longitudinal plane wave with a circular crack imbedded in a porous medium is considered [5], and the problem is formulated in dual integral equations for the Hankel transform of the wave field. The formation mechanism of "water film" (or crack) in saturated sand is analyzed theoretically and numerically[6]. The cracks in fluid-saturated two-phase medium is explored [7] by finite element method. A circular crack imbedded in a porous medium under a normally incident time-harmonic longitudinal plane wave is studied by second kind single Fredholm integral equation[8]. A finite element algorithm is presented for the numerical modeling of cohesive fracture in a partially saturated porous media[9]. The saturated cracks in 4% porosity Fontainebleau sandstone fro an effective mean pressure ranging from 2 to 95MPa under high ultrasonic frequencies, Vp/Vs, ratio is explored [10]. The narrow distribution of cavities permeability model is devised combining the hydraulic radium and percolation concepts [11]. But this problem is far from solved for complex relationship between fluid states, physical properties of tight sandstone and ultra high temperature-pressure (UHTP). There are four differences between classical porous medium and tight sandstone. First, the pore/void size is located at atom-molecular-pico-nano scale level, the fluid viscous (as function of UHTP), the effects of boundary layer, and the unsteady fluid flow (eddy flow and turbulent flow) can not be neglected; Second, when the P-T conditions are high enough, the water role in the rock/mineral includes free-supercritical-constitutional state, the fluid flow particles are composed of four components [H2O, H+, (OH)-, (H3O)+]. Third, the micro pore is composed of four types [multi-grain gap, polycrystalline space, crystal space and crystal internal space] and the deformation of the micro-structure had to be considered; Last, the fluid flow permeability and diffusion include intermolecular collisions and diffusion (Fick's laws of diffusion), molecular collisions with interface (Knudsen diffusion), molecular and interfacial adhesive and viscous flow (Darcy and Forchheimer flow). With the scale decrease, the surface stress component became domain, the effect of the body stress component reducing, and the classical N-S equation is no longer applies.

In this work, based on the previous work on saturated dislocation transient propagation-evolution in olivine structure under ultra-high temperature and pressure (UHTP)[12], and general solutions of extended displacement (elastic displacement, electrical potential, magnetic potential and thermal potential) given in the previous work[13, 14], the three-dimensional pore-network crack transient Hydrofracturing-liquefaction in tight sandstone (3D PC-TH-TS) under seismic waves & electro-magneto-thermo-elastic fields is studied by using lattice Boltzmann & finite element & hypersingular integral equation (LB-FE-HIE) on parallel GPU-CPU environment.

First, the 3D PN-TH-TS problem is reduced to solving a set of LB-FE-HIEs coupled with extended boundary integral equations by using the Green functions and distribution functions, in which the

unknown functions are the extended pore-network cracks displacement discontinuities. Then, the behavior of the extended displacement discontinuities around the pore-network cracks surface terminating at the solid-liquid film interface are analyzed by the extended hypersingular integral main-part analysis method of LB-FE-HIEs. Analytical solutions for the extended singular dynamic stresses, the extended dynamic stress intensity factors and the extended dynamic energy release rate near the dislocations front are provided. Thrid, the tight sandstone sample from the Ordos Basin Triassic formation is selected and different tomography resolution data is obtained by X-ray CT digital technology, the fluid-solid coupled porous medium physical modeling is established, and the relatively Hydrofracturing-liquefaction numerical modelling of tight sandstone is obtained for the first time. Last, The simulations of 3D PC-TH-TS process is presented, the hydrofacturing-liquefaction varying with the amplitude, frequency and time of earthquake wave is obtained. The relationship between the tight sandstone pore-network cracks transient propagation-evolution and the maximum tight sandstone fracturing-liquefaction stress criteria is explored.

2. Basic equations

Here summation from 1 to 3(1 to 6) over repeated lowercase (uppercase) subscripts is assumed, and a subscript comma denotes the partial differentiation with respect to the coordinates. The ultralow permeability tight sandstone (UPTS) consists of six constituents, i.e. the particles of solid skeleton (the 1st component), bound liquid film (the 2nd component), static pore-liquid (the 3rd component, free state water), dynamic pore-liquid I (the four component, free state water), dynamic pore-liquid II (the five component, supercritical state water) and dynamic pore-liquid III (the 6th component, constitutional state water [H+, (OH)-, (H3O)+]. The governing equations and constitutive relations of UPTS under EMTE field can be expressed as [15, 16],

$$A_L \tau^L_{ij,j} + B_L + \Sigma_{iJ,i} + f_J = 0 \tag{1}$$

where

$$A_L = \begin{cases} 1-(1-\alpha)\kappa & L=1 \\ \phi_2^P & L=2 \\ \phi_3^P & L=3 \\ \phi_4^P & L=4 \\ \phi_5^P & L=5 \\ \phi_6^P & L=6 \end{cases} \qquad B_L = \begin{cases} \left[(1-\kappa)\rho_1 + \alpha\kappa\rho_2\right]\ddot{U}(x_i,t)_{1i} - \sum_{N=1}^{5}\left\{v_N\delta_N^2\chi^{-1}\chi_N^{-1}\left[\dot{U}(x_i,t)_{(N+1)i} - \dot{U}(x_i,t)_{Ni}\right]\right\} & L=1 \\ \phi_2^P\rho_2\ddot{U}(x_i,t)_{2i} - \sum_{N=2}^{5}\left\{v_N\delta_N^2\chi^{-1}\chi_N^{-1}\left[\dot{U}(x_i,t)_{(N+1)i} - \dot{U}(x_i,t)_{Ni}\right]\right\} & L=2 \\ \phi_3^P\rho_3\ddot{U}(x_i,t)_{3i} - \sum_{N=3}^{5}\left\{v_N\delta_N^2\chi^{-1}\chi_N^{-1}\left[\dot{U}(x_i,t)_{(N+1)i} - \dot{U}(x_i,t)_{Ni}\right]\right\} & L=3 \\ \phi_4^P\rho_4\ddot{U}(x_i,t)_{4i} - \sum_{N=4}^{5}\left\{v_N\delta_N^2\chi^{-1}\chi_N^{-1}\left[\dot{U}(x_i,t)_{(N+1)i} - \dot{U}(x_i,t)_{Ni}\right]\right\} & L=4 \\ \phi_5^P\rho_5\ddot{U}(x_i,t)_{5i} - v_5\delta_5^2\chi^{-1}\chi_5^{-1}\left[\dot{U}(x_i,t)_{6i} - \dot{U}(x_i,t)_{5i}\right] & L=5 \\ \phi_6^P\rho_6\ddot{U}(x_i,t)_{6i} + v_6\delta_6^2\chi^{-1}\chi_6^{-1}\dot{U}(x_i,t)_{6i} & L=6 \end{cases}$$

$U(x_i,t)_{i1}, U(x_i,t)_{i2}, U(x_i,t)_{i3}, U(x_i,t)_{i4}, U(x_i,t)_{i5}$ and $U(x_i,t)_{i6}$ denote the components of displacements of drained porous solid frame, the components of displacements of drained bound liquid film, denote the components of displacements of the static pore-liquid, the components of displacements of the dynamic pore-liquid I, the components of displacements of the dynamic pore-liquid II, and the components of displacements of the dynamic pore-liquid III respectively; ρ_L, v_{NL}, χ, χ_{NL} and δ_L denote density, viscosity, intrinsic permeability, relative permeability and volume fractions of L th component of ultra-low permeability porous rock respectively; κ, α, ϕ_2^P, ϕ_3^P, ϕ_4^P, ϕ_5^P and ϕ_6^P represent macro porosity of ultra-low permeability rock, fraction occupied by bound liquid film, the connected porosity of bound liquid film, the connected porosity of static pore-liquid part, the connected porosity of dynamic pore-liquid I, II and III respectively. In addition, the extended stress displacement matrix tensor and the extended body load vector, $\sum_{iJ}$ and f_J, are defined respectively as

$$\sum_{iJ}=\begin{cases}\sigma_{ij} & J=j=1,2,3\\ D_i & J=4\\ B_i & J=5\\ \vartheta_i & J=6\end{cases}\qquad f_J=\begin{cases}f_j & J=j=1,2,3\\ -f_e & J=4\\ -f_m & J=5\\ -f_\vartheta & J=6\end{cases}\tag{2}$$

The combined constitutive equation is written as

$$\sum_{iJ}=E_{iJKl}Z_{Kl}\tag{3}$$

where the EMTE constant matrix tensor and the extended strain field matrix tensor, E_{iJKl} and Z_{Kl}, take the form

$$E_{iJKl}=\begin{bmatrix}C_{iJKl} & -\Pi_{iJ} & 0\\ 0 & 0 & -\lambda_{iJ}\end{bmatrix}\qquad Z_{Kl}=[\ U^s_{K,l}\quad \Upsilon_{,l}\ ]^T\tag{4}$$

The extended elastic stiffness tensor, the extended thermal stress constants tensor and the extend elastic displacement vector, C_{iJKl}, Π_{iJ} and U_K, are defined as

$$C_{iJKl}=\begin{cases}c_{ijkl} & J,K=1,2,3\\ e_{lij} & J=1,2,3;K=4\\ e_{ikl} & J=4;K=1,2,3\\ d_{lij} & J=1,2,3;K=5\\ d_{ikl} & J=5;K=1,2,3\\ -g_{il} & J=4;K=5 or J=5;K=4\\ -\in_{il} & J,K=4\\ -\mu_{il} & J,K=5\end{cases}\quad \Pi_{iJ}=\begin{cases}\iota_{ij} & J=1,2,3;K=6\\ \varsigma_{il} & J=4;K=6\\ \eta_{il} & J=5;K=6\end{cases}\quad U^s_K=\begin{cases}u^s_i & K=1,2,3\\ \phi^s_4 & K=4\\ \varphi^s_5 & K=5\\ \Upsilon^s_6 & K=6\end{cases}\tag{5}$$

σ_{ij}, D_i, B_i, ϑ_i, f_i, f_e, f_m , f_ϑ, c_{ijkl}, e_{lij}, d_{lij}, $\in_{il}$, g_{il}, μ_{il}, ι_{ij}, ς_{il}, η_{il}, λ_{ij}, u^s_i, ϕ^s_4, φ^s_5 and Υ^s_6 are defined in [14]. The drained porous solid frame and the drained bound liquid film have the same displacement and pressure; The static pore-liquid, the dynamic pore-liquid I have the same displacement; The pressure of saturated porous solid frame is the sum of static pore-liquid, dynamic pore-liquid I, dynamic pore-liquid II and dynamic pore-liquid III components pressure. The seismic wave displacement in ultra-low permeability porous rock can be written as

$$U(x_i,t)_{iL}=\Phi^1(x_i,t)_{iL,i}+\varepsilon_{ijk}\Phi^2(x_i,t)_{jL,k}$$

where

$$\Phi(x_i,t)^\alpha_{iL}=-A^\alpha_i E(\omega t)\left\{\delta_{3i}\begin{bmatrix}E(-2\omega^\alpha_L x_1x_2x_3\sin\theta^\alpha_{1L}\cos\theta^\alpha_{2L})+E(-2\omega^\alpha_L x_1x_2x_3\cos\theta^\alpha_{1L}\sin\theta^\alpha_{2L})\\ +E(-2\omega^\alpha_L x_1x_2x_3\cos\theta^\alpha_{1L}\cos\theta^\alpha_{2L})+E(-2\omega^\alpha_L x_1x_2x_3\sin\theta^\alpha_{1L}\sin\theta^\alpha_{2L})\end{bmatrix}\right\}$$
$$\begin{bmatrix}+E(-2\omega^\alpha_L x_3\cos\angle(x_3,x_2)^\alpha_{pL})+E(-2\omega^\alpha_L x_3\cos\angle(x_3,x_1)^\alpha_{pL})\end{bmatrix}$$
$$\times\begin{bmatrix}E(\omega^\alpha_L x_1\sin\angle(x_3,x_2)^\alpha_{pL})+E(\omega^\alpha_L x_2\sin\angle(x_3,x_1)^\alpha_{pL})+E(2\omega^\alpha_L x_1x_2\sin\theta^\alpha_{1L}\cos\theta^\alpha_{2L})+E(2\omega^\alpha_L x_1x_2\cos\theta^\alpha_{1L}\sin\theta^\alpha_{2L})\\ +E(2\omega^\alpha_L x_1x_2\cos\theta^\alpha_{1L}\cos\theta^\alpha_{2L})+E(2\omega^\alpha_L x_1x_2\sin\theta^\alpha_{1L}\sin\theta^\alpha_{2L})\end{bmatrix}$$

$$\theta^\alpha_{1L}=\begin{cases}\angle(x_3,x_2)_{pL}+\angle(x_3,x_1)_{pL} & \alpha=1\\ \angle(x_3,x_2)_{pL}-\angle(x_3,x_1)_{pL} & \alpha=2\end{cases},\ \theta^\alpha_{2L}=\begin{cases}\angle(x_3,x_2)_{sL}+\angle(x_3,x_1)_{sL} & \alpha=1\\ \angle(x_3,x_2)_{sL}-\angle(x_3,x_1)_{sL} & \alpha=2\end{cases},\ \omega^\alpha_L=\begin{cases}\omega/v^L_P & \alpha=1\\ \omega/v^L_S & \alpha=2\end{cases},\ E()=e^{i()}$$

v^1_P, v^2_P, v^3_P, v^4_P, v^5_P and v^6_P denote the P-wave velocity in drained porous solid frame, drained bound liquid film, static pore-liquid, dynamic pore-liquid I, dynamic pore-liquid II and dynamic pore-liquid III respectively; v^1_S, v^2_S, v^3_S, v^4_S, v^5_S and v^6_S denote the P-wave velocity in drained porous solid frame, drained bound liquid film, static pore-liquid, dynamic pore-liquid I, dynamic pore-liquid II and dynamic pore-liquid III respectively; $\angle(x_3,x_2)_{pL}$, $\angle(x_3,x_1)_{pL}$, $\angle(x_3,x_2)_{sL}$ and $\angle(x_3,x_1)_{sL}$ denote the P-wave incidence angle between x_3 and x_2 axes, the P-wave incidence angle between x_3 and x_1 axes, the S-wave incidence angle between x_3 and x_2 axes and the S-wave incidence angle between x_3 and x_1 axes in the L th component of ultra-low permeability porous rock

respectively. If we defined that solid skeleton component and liquid components are parallel and subjected to the same strain, the time-dependent rigidity modulus components G_L of ultra-low permeability porous rocks can be defined as

$$G_L = (1-f)G_0 + \alpha f (v_s^L \varepsilon_L^{-2})_{,t}$$

f, α, ε_L^{-2} and G_0 represent macro-porosity of ultra-low permeability porous rocks, fraction occupied by bound liquid film, non-dimensional parameter (linked fluid viscosity, bulk modulus, density and permeability) of L th component of ultra-low permeability porous rock, and rigidity modulus of solid grains.

3.LB-FE-HIE for 3D PC-TH-TS under seismic wave & electro-magneto-thermo-elastic fields

3.1 Lattice Boltzmann & finite element (LB-FE) coupled modeling

It is shown in the Fig 1, The LB-FE coupled modeling for tight sand porous media is established. The finite element method is using to analyze solid sketch part of the porous tight sand (the strain/strain rate-stress/stress rate-temporal spatial solid sketch structure-macro strength) (Fig1D, 1E); D3Q27 lattice Boltzmann method is using to analyze fluid pore part of the porous tight sand (fluid stress-viscous-density-time-bulk strain) (Fig 1F); LB-FE coupled modeling can deal with interface stress-strain between solid sketch and fluid pore (surface of pore-network cracks) (Fig 1C). In our work, the three-dimensional 20 node arbitrary hexahedral element (3D-20 Hexahedral element) is defined for the solid sketch part of the porous tight sand, and the three-dimensional 27 particle arbitrary hexahedral node (D3Q27) is defined for the fluid pore part of the porous tight sand; if the element is located at the surface of the pore-network cracks, then we defined that each D3Q27 node has the same physical meaning as one arbitrary node of 3D-20 Hexahedra element (Fig 1G,1H and 1I), the distribution function of lattice Boltzmann and the shape function in finite element can be linked through intricate theoretical formulation, and the LB-FE coupled fluid pore-solid sketch porous modeling can be established, the theoretical derivation can be written as follows,The equation of shape function for 3D-20 Hexahedra isoparametric element is defined as

$$N_k = \begin{cases} \prod_{i=1}^{3}(1+x_{ik}x_i)\left(\sum_{i=1}^{3}x_{ik}x_i - 2\right) & k = 1 \sim 8 \\ 2\prod_{i=1}^{3}(1+x_1^2) & k = 9 \sim 12 \\ 2(1-x_2^2)(1+x_{ik}x_1)(1+x_{3k}x_3) & k = 13 \sim 16 \\ 2(1-x_3^2)(1+x_{1k}x_1)(1+x_{3k}x_3) & k = 16 \sim 20 \end{cases} \tag{6}$$

The relatively stiffness matrix for 3D-20 Hexahedra isoparametric element is defined as

$$[K] = \int_{-1}^{1}\int_{-1}^{1}\int_{-1}^{1}[B]^T[D][B]\lfloor J \rfloor dx_1 dx_2 dx_3 \tag{7}$$

where

$$[B_K] = \begin{bmatrix} \frac{\partial N_K}{\partial \xi_1} & 0 & 0 \\ 0 & \frac{\partial N_K}{\partial \xi_2} & 0 \\ 0 & 0 & \frac{\partial N_K}{\partial \xi_3} \\ \frac{\partial N_K}{\partial \xi_2} & \frac{\partial N_K}{\partial \xi_1} & 0 \\ 0 & \frac{\partial N_K}{\partial \xi_1} & \frac{\partial N_K}{\partial \xi_2} \\ \frac{\partial N_K}{\partial \xi_3} & 0 & \frac{\partial N_K}{\partial \xi_1} \end{bmatrix} \quad [D] = \frac{E(1-v)}{(1+v)(1-2v)}\begin{bmatrix} 1 & A_1 & A_2 & 0 & 0 & 0 \\ A_1 & 1 & A_1 & 0 & 0 & 0 \\ A_2 & A_1 & 1 & 0 & 0 & 0 \\ 0 & 0 & 0 & A_2 & 0 & 0 \\ 0 & 0 & 0 & 0 & A_2 & 0 \\ 0 & 0 & 0 & 0 & 0 & A_2 \end{bmatrix} \quad [J] = \begin{bmatrix} \frac{\partial \xi_1}{\partial x_1} & \frac{\partial \xi_2}{\partial x_1} & \frac{\partial \xi_3}{\partial x_1} \\ \frac{\partial \xi_1}{\partial x_2} & \frac{\partial \xi_2}{\partial x_2} & \frac{\partial \xi_3}{\partial x_2} \\ \frac{\partial \xi_1}{\partial x_3} & \frac{\partial \xi_1}{\partial x_3} & \frac{\partial \xi_1}{\partial x_3} \end{bmatrix} \quad A_1 = \frac{v}{1-v} \quad A_2 = \frac{1-2v}{2(1-v)}$$

The extended equivalent stress and tension for 3D-20 Hexahedra isoparametric element is defined as

$$\{R\}_{volume} = \int_{-1}^{1}\int_{-1}^{1}\int_{-1}^{1}[N]^T\{p\}|J|dx_1dx_2dx_3 \tag{8}$$

$$\{R\}_{surface} = \iint_{A_{x_1x_2}}[N]^T\{\bar{p}\}\Big|_{x_1=1}dA \tag{9}$$

Take the distribution function of D3Q27 LB node[17] into the shape function of 3D-20 Hexahedra element, the LB-FE modeling can be established to analyze the fluid-solid coupled porous structure problem.

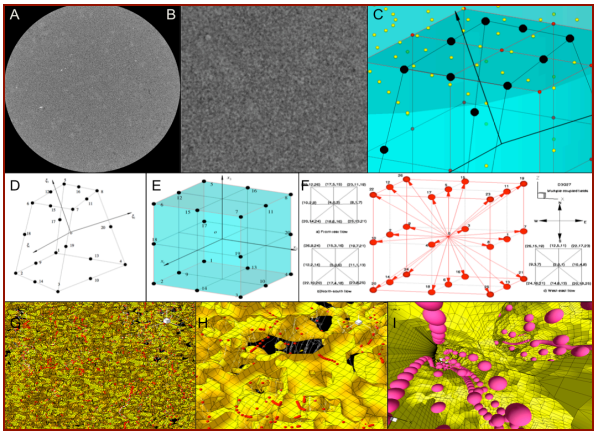

Fig 1. The lattice Boltzmann & finite element fluid-solid coupled modeling
Fig 1A. Cross-section of rock CT scan digital data, Fig 1B. Cross-section of digital rock, Fig 1C. LBM & FEM fluid-solid coupled modelling
Fig 1D, Sketch of 20 nodes FEM cell, Fig 1E. Sketch of 20 nodes isoparametric FEM cell, Fig 1F Sketch of D3Q27 LBM grid point
Fig 1G. Micro structure of tight rock (Scale I), Fig 1H. Micro structure of tight rock (Scale II), Fig 1I Micro structure of tight rock (Scale III)

3. 2 LB-FE-HIE for 3D PC-TH-TS under seismic wave & electro-magneto-thermo-elastic fields

Using Micro XCT-400 CT system, the high resolution data are obtained, the 3D virtual digital rock are reestablished, and the LB-FE-HIE physical model are constructed; The threshold is arrange from 78~100, the interior geometry structure at low level scales translate from the pix RGB color into the cell-mesh-grid model, the initial/boundary conditions, the physical/chemical parameters of rock and water, and the low level scales geometry pore-solid structure can be defined.

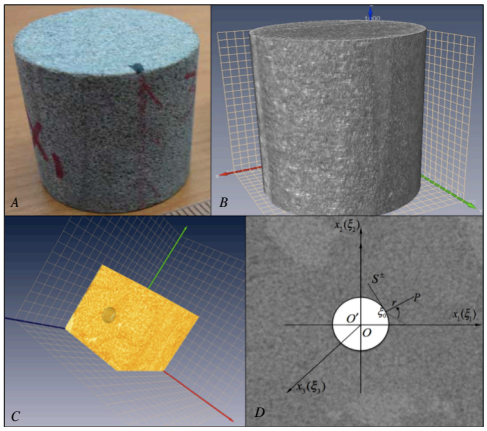

Fig 2. The tight sandstone transient hydrofracturing-liquefaction lattice Boltzmann & finite element fluid-solid coupled modelling
Fig 2A. Sample of tight sandstone, Fig 2B. Virtual digital rock sample of tight sandstone
Fig 2C, A circle drilling in the tight sandstone, Fig 1D. Sketch of transient hydrofracturing-liquefaction in the tight sandstone

Fig 2. shows the PC-TD-TS LB-FE-HHIE coupled modeling, the diameter and the length of the core samples are equal to 5cm and 10cm respectively; the resolution of cross-section and the interval between cross-sections are equal to 10μm. The general model was formulated by utilizing an automatic local amplification grid technique, and the initial LB-FE-HIE physical model is equal to 1024×1024×1024 pixels, which does not include the extended variables. Applying function in references [18, 19] to the initial virtual digital rock modeling, we can obtained the random LB-FE-HIE modeling (decreasing the computational scale in parallel CPU-GPU environment). The pore/void size is located at atom-molecular-pico-nano scale level, the fluid viscous (as function of

pressure-temperature), the effects of boundary layer, and the unsteady fluid flow (eddy flow and turbulent flow) had to be considered. The water role in the rock includes free state, supercritical state and constitutional state; the fluid flow particles are composed of four components [H2O, H+, (OH)-, (H3O)+]. The micro pore is composed of four kinds [multi-grain gap, polycrystalline clearance, crystal space and crystal internal clearance] and the deformation of the microstructure had to be considered. The fluid flow permeability and diffusion include intermolecular collisions and diffusion (Fick's laws of diffusion); molecular collisions with interface (Knudsen diffusion), molecular and interfacial adhesive and viscous flow (Darcy flow and Forchheimer flow). With the scale decrease, the surface stress component became domain, the effect of the body stress component reducing, and the classical N-S equation is no longer applies. The more detailed introduction can be found elsewhere in the literature[20-23].

Consider the tight sandstone containing a random three-dimensional transient hydrofacturing-liquefaction crack as shown in Fig.2D. A fixed global rectangular Cartesian system x_i (i=1,2,3) is chosen. Assume that the pore-network crack S ($S^+ \bigcup S^-$) is subjected to remote the seismic wave mechanical loads $p_j(P,Q,t)$, the seismic wave electrical loads $q(P,Q,t)$, the seismic magnetic loads $b(P,Q,t)$ and the thermal loads $\rho(P,Q,t)$, respectively. The local rectangular Cartesian system ξ_i are chosen, the stochastic flaws are assumed to be in the $\xi_1\xi_2^i$ plane and normal to the ξ_3 axis. Using the EMTE form of the Somigliana identity, the extended displacement vector, $U_I(p)$, at interior point $p(x_1,x_2,x_3)$ is expressed as

$$U_I(p)=\int_{S^+}(U_{IJ}(p,q)T_J(q)-T_{IJ}(p,q)U_J(q))ds(q)-\int_{\Gamma}(T_{IJ}(p,q)U_J(q)+U_{IJ}(p,q)T_J(q))ds(q)+\int_{\Omega}U_{IJ}(p,q)f_J(q)ds(q) \tag{10}$$

where Ω is the domain occupied by the EMTE-CMCs, Γ is the external boundary, $T_J(q)$ is the extended elastic tractions on boundaries, $U_{IJ}(p,q)$ and $T_{IJ}(p,q)$ are the fundamental solutions. Using constitutive Equation (10), the corresponding extended stresses tensor, Σ_{IJ}, is expressed as

$$\Sigma_{IJ}(p)=-\int_{S^+}S_{KiJ}(p,q)\tilde{U}_K(q)ds(q)+\int_{\Gamma}(D_{KiJ}(p,q)T_K(q)-S_{KiJ}(p,q)U_K(q))ds(q)+\int_{\Omega}D_{KiJ}(p,q)f_K(q)ds(q) \tag{11}$$

The kernels functions, S_{KiJ} and D_{KiJ}, are as follows:

$$S_{KiJ}(p,q)=-E_{iJMn}T_{MK,n}(p,q) \qquad D_{KiJ}(p,q)=-E_{iJMn}U_{MK,n}(p,q) \tag{12}$$

The hypersingular integral equations can be obtained as

$$\sum_{i=1}^{5}\rho_i^2t_i^2\sum_{m=3}^{6}\tilde{u}_{m,1}=\int_{S^+}\left(\frac{c_{44}^2D_0s_0^2(\delta_{\bar{\alpha}\bar{\beta}}-3r_{,\bar{\alpha}}r_{,\bar{\beta}})+(\delta_{\alpha\beta}-3r_{,\alpha}r_{,\beta})\sum_{i=1}^{5}\rho_i^2t_i^2}{r^3}\hat{K}\,\tilde{u}_{\beta}+\frac{3r_{,\alpha}\sum_{i=1}^{5}\lambda_{33}s_i^2t_i}{r^4}\tilde{u}_6\right)ds+\int_{S^+}K_{\alpha i}\tilde{u}_i\,ds=-p_{\alpha} \tag{13}$$

$$\sum_{n=3}^{5}\sum_{i=1}^{5}\rho_i^mt_i^t\sum_{m=3}^{6}\tilde{u}_{m,2}+\int_{S^+}\left(\frac{r_{,\alpha}\sum_{i=1}^{5}A_i^{\Upsilon}t_i^2\rho_i^1}{r^2}\tilde{u}_{\alpha}+\frac{\sum_{n=3}^{5}\sum_{i=1}^{5}\rho_i^mt_i^t}{r^3}\tilde{u}_n+\frac{3\lambda_{3\alpha}r_{,\alpha}\sum_{i=1}^{5}s_i^2\lambda_i^{\vartheta}\rho_i^m}{r^4}\tilde{u}_6\right)ds+\int_{S^+}K_{mi}\tilde{u}_i\,ds=-p_m \tag{14}$$

$$\sum_{i=1}^{5}A_i^{\Upsilon}\lambda_{3\beta}t_i^2\tilde{u}_{\alpha,\alpha}+\int_{S^+}\left(\frac{(\delta_{\alpha\beta}-3r_{,\alpha}r_{,\beta})\sum_{i=1}^{5}A_i^{\Upsilon}\lambda_{3\beta}t_i^2}{r^2}\tilde{u}_{\beta}+\frac{3\lambda_{3\alpha}r_{,\alpha}\sum_{i=1}^{5}A_i^{\Upsilon}s_i^2\lambda_i^{\vartheta}\lambda_{33}\rho_i^6}{r^4}\tilde{u}_6\right)ds+\int_{S^+}K_{6i}\tilde{u}_i\,ds=-p_6 \tag{15}$$

where $p_i^{\hat{i}}$, $p_4^{\hat{i}}(q^{\hat{i}})$, $p_5^{\hat{i}}(b^{\hat{i}})$ and $p_5^{\hat{i}}(\rho^{\hat{i}})$ can obtained from the solution for the loads of the solids.

4. Dynamic stress, dynamic stress intensity factors and energy release rate near the dislocations front

In order to investigate the singularity of the dislocations front, consider a local coordinate system defined as $x_1\ x_2\ x_3$. The x_1-axis is the tangent line of the dislocation front at point q_0, x_2-axis is the internal normal line in the dislocation plane, and x_3-axis is the normal of the dislocation. Then, the extended displacement discontinuities of the dislocation surface near a dislocation front point q_0 can be assumed as

$$[\ \tilde{u}_i^{\hat{I}}(q)\quad \tilde{\phi}^{\hat{I}}(q)\quad \tilde{\varphi}^{\hat{I}}(q)\quad \tilde{\Upsilon}^{\hat{I}}(q)\ ] = g_k^{\hat{I}}(q_0)\xi_2^{\lambda_k} \qquad 0 < Re(\lambda_k) < 1 \tag{16}$$

where $g_k(q_0)$ and λ_k represent non-zero constants and singular index, respectively. The dynamic stress intensity factors are defined as

$$K_1^{\hat{I}} = \lim_{r\to 0}\sqrt{2r}\sigma_{33}^{\hat{I}}(r,\theta)\Big|_{\theta=0}, K_2^{\hat{I}} = \lim_{r\to 0}\sqrt{2r}\sigma_{32}^{\hat{I}}(r,\theta)\Big|_{\theta=0}, K_3^{\hat{I}} = \lim_{r\to 0}\sqrt{2r}\sigma_{31}^{\hat{I}}(r,\theta)\Big|_{\theta=0} \tag{17}$$

$$K_4^{\hat{I}} = \lim_{r\to 0}\sqrt{2r}D_3^{\hat{I}}(r,\theta)\Big|_{\theta=0}, K_5^{\hat{I}} = \lim_{r\to 0}\sqrt{2r}B_3^{\hat{I}}(r,\theta)\Big|_{\theta=0}, K_6^{\hat{I}} = \lim_{r\to 0}\sqrt{2r}\vartheta_3^{\hat{I}}(r,\theta)\Big|_{\theta=0} \tag{18}$$

where r is the distance from point p to the dislocation front point q_0, the dynamic stress around the dislocation front can be expressed as follows

$$\sigma_{13}^{\hat{I}} = c_{44}^2 D_0 s_0^2 \frac{\pi g_1^{\hat{I}}}{\sqrt{rr_0}}\cos\frac{\theta_0}{2} \tag{19}$$

$$\begin{aligned}\sigma_{23}^{\hat{I}} = \sum_{i=1}^{5}\frac{\pi}{\sqrt{rr_i}}\{&g_6^{\hat{I}}\lambda_{33}[15\lambda_{33}s_i^2\cot\theta_i(3\cos\frac{\theta_i}{4}-3\sin^2\frac{\theta_i}{2}\cos\frac{\theta_i}{2}-\frac{1}{4}\sin^2\theta_i\cos\frac{3\theta_i}{2})-\frac{2\lambda_{33}}{r^2r_i^2}\sin^{-1}\frac{\theta_i}{2}\\ &+\frac{\lambda_{32}}{2rr_i\sin\theta}(2\cos^{-1}\frac{\theta_i}{2}-3\cos\frac{\theta_i}{2}-\cos\frac{5\theta_i}{2})]+\rho_i^2\pi\cos\frac{\theta_i}{2}(t_2g_2+4\sum_{m=3}^{5}t_i^m g_m^{\hat{I}})\}\end{aligned} \tag{20}$$

$$\begin{aligned}\dot{\sigma}_{3n}^{\hat{I}} = \sum_{i=1}^{5}\rho_i^n s_i\pi[&\frac{1}{\sqrt{rr_i}}(t_i^2 g_2^{\hat{I}}\cot\theta_i\cos^{-1}\frac{\theta_i}{2}+6\cot\frac{\theta_i}{2}\sum_{m=3}^{5}t_i^m g_m^{\hat{I}})+g_6^{\hat{I}}s_i\lambda_i^{\vartheta}\sqrt{rr_i}\cot\theta_i\cos\frac{\theta_i}{2})]\\ &+2\pi A_i^{\Upsilon}\mathfrak{t}_{33}[\sqrt{rr_i}\cos\frac{\theta_i}{2}(g_2^{\hat{I}}\cot\theta_i+\sum_{m=3}^{5}t_i^m g_m^{\hat{I}})+\frac{s_i^2\lambda_{33}\lambda_i^{\vartheta}g_6^{\hat{I}}}{\sqrt{rr_i}}\cos\frac{\theta_i}{2}],n=3-5\end{aligned} \tag{21}$$

$$\begin{aligned}\vartheta_3^{\hat{I}} = \sum_{i=1}^{5}\frac{A_i^{\Upsilon}\pi}{\sqrt{rr_i}}&[\cos\frac{\theta_i}{2}(\lambda_{32}+4\lambda_{33}s_i^2)\sum_{m=2}^{5}t_i^m g_m^{\hat{I}}+\frac{4\lambda_{32}t_i^2 g_2^{\hat{I}}s_i^2\lambda_i^{\vartheta}}{3}(2\lambda_{32}\cos\frac{\theta_i}{2}+\frac{3\lambda_{33}}{r^2r_i^2}\sin^{-1}\frac{\theta_i}{2})\\ &15rr_i g_6^{\hat{I}}\lambda_{32}s_i^2\lambda_i^{\vartheta}\cot\theta_i(3\cos\frac{\theta_i}{4}-6\cos\frac{\theta_i}{2}\sin^2\frac{\theta_i}{2}-\frac{1}{4}\sin^2\theta_i\cos\frac{3\theta_i}{2})(2s_i^2\lambda_{33}+\frac{\lambda_{32}}{rr_i\sin\theta_i})]\end{aligned} \tag{22}$$

The extended singular stresses, $\dot{\sigma}_{3n}^{\hat{I}} = [\ \sigma_{33}^{\hat{I}}\quad D_3^{\hat{I}}\quad B_3^{\hat{I}}\ ]$, can be rewritten as

$$\sigma_{13}^{\hat{I}} = K_3^{\hat{I}}\cos\frac{\theta_0}{2}/\sqrt{2rr_0} \tag{23}$$

$$\hat{\sigma}_{n3}^{\hat{I}} = [\quad \sigma_{23}^{\hat{I}}\quad \sigma_{33}^{\hat{I}}\quad D_3^{\hat{I}}\quad B_3^{\hat{I}}\quad \vartheta_3^{\hat{I}}\quad] = (K_1^{\hat{I}}f_{n1}+K_2^{\hat{I}}f_{n2}+K_4^{\hat{I}}f_{n4}+K_5^{\hat{I}}f_{n5}+K_6^{\hat{I}}f_{n6})/\sqrt{2r}, n=2-6 \tag{24}$$

where the coefficient functions f_{IJ} are listed in [14]. Other extended singular stresses near point q_0 can also be obtained by use of above method. $K_2^{\hat{I}}$ is coupled with $K_3^{\hat{I}}$ and $K_6^{\hat{I}}$, $K_1^{\hat{I}}$ is coupled with $K_4^{\hat{I}}$, $K_5^{\hat{I}}$ and $K_6^{\hat{I}}$. The energy release rate can be obtained and expressed as followings,

$$\frac{dW}{dV} = 2\sqrt{2r}S = \frac{K_n^2}{2\sqrt{2r}}\left(\frac{a_{3n}^2}{E}+\frac{a_{1n}^2+a_{2n}^2}{\tilde{\mu}}+\frac{a_{4n}^2+a_{5n}^2+a_{6n}^2}{E'}\right) \tag{13}$$

$$W = U_s + U_k + U_f \tag{14}$$

5. Numerical simulation and discussion

A tight sandstone core samples from the Ordos Basin Triassic formation of China which include multi pore-network cracks is selected, the rock depth, the diameter, the length, the density, the confining pressure, the pore stress and the temperature are defined as 862.76~864.36m, 25.4mm, 25~30mm, 2.359~2.426g/cm3, 0~200MPa, 0~10MPa, 35~45 °C respectively, the more detail parameters of the tight sandstone core sample are shown in Tab.1.

Tab.1. Mineral composition, porosity and matrix density of the tight sandstone samples

Sample Number	Direction	Mineral composition(volume percent)					Porosity (%)	Density (g/cm^3)
		Quarzt	Feldspar	Rock debris	Mica	Heavy placer mineral		

	X1	24.34	63.05	8.17	3.73	0.71	8.216	2.368
S1	Y1	23.05	63.16	9.98	3.63	0.18	6.744	2.359
	Z1	28.66	61.36	7.95	0.16	1.87	6.992	2.379
	X2	33.33	57.43	9.24	-	-	6.252	2.426
S2	Y2	27.93	61.39	10.68	-	-	6.822	2.384
	Z2	23.42	56.32	12.08	8.18	-	7.649	2.379
	X3	34.05	57.93	7.83	-	0.19	7.017	2.374
S3	Y3	29.14	58.48	11.43	-	0.95	7.333	2.379
	Z3	26.36	58.53	13.56	-	1.55	6.918	2.382

5.1 Hydrofacturing-liquefaction process varying with the frequency of earthquake wave

The pore-network cracks transient hydrofacturing-liquefaction as function of the frequency of the earthquake wave is shown in Fig. 3. At the fixed amplitude and constituting time, the dynamic fluid stress act on the tight sandstone as electromagnetic wave and stress wave, at the range of 10Hz～100Hz, the surface of pore-network cracks do not appear liquefaction phenomena, even the surface of pore-net-work cracks began propagation and hydrofacturing phenomena appears; with the frequency increasing, when it reach to 200Hz～300Hz, the hydrofacturing phenomena is domain and some pore-network cracks zone of the tight sandstone appear hydrofacturing-liquefaction phenomena, and the constituting time and amplitude decreasing with the frequency increased, the constituting time is around 10E-5s and no draining phenomena appears during hydrofacturing-liquefaction process..

When the frequency is lower than 10Hz, the dynamic fluid stress act on the tight sandstone as quasi-static pore hydrostatic stress, and accompanying draining phenomena in the hydrofacturing failure progress; the maximum tight sandstone fracturing-liquefaction stress is the criteria which leading the hydrofacturing failure.

In general, the low frequency part of the earthquake wave act on the tight sandstone as static/quasi-static style, when the maximum principle stress is reach to the tight sandstone strength criteria, the pore-network cracks begin propagation and accompanying with draining process, no liquefaction appearing for do not reach the maximum micro tight sandstone structure strength limit; the dynamic stress released sharply with the distance between the surface of cracks, we defined it as crack surface frequency earthquake wave or near-field (around the crack surface) frequency earthquake wave.

The high frequency part of the earthquake wave act on the tight sandstone as transient electromagnetic wave and stress wave, the constituting time is very short and no draining accompanied in the whole process; the high frequency energy reach the maximum micro tight sandstone structure strength limit and destroy the tight micro pore-network structure in 10E-5s (Non-connected pore throat destruction); when the frequency is exceed to 400Hz, the electromagnetic wave can leading pore stress oscillation sharply and make the transient liquefaction appear in the whole tight sandstone zone, without draining and hydrofacturing process.

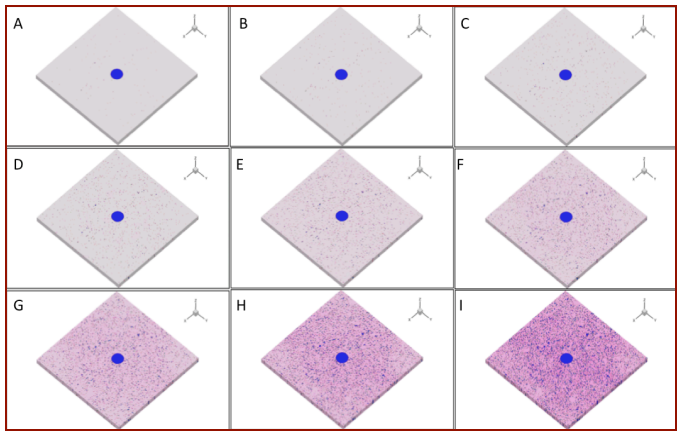

Fig 3. The transient hydrofracturing-liquefaction process as function of frequency of earthquake wave
Fig3A. Frequency is 10Hz, Fig3B. Frequency is 50Hz, Fig3C. Frequency is 100Hz
Fig3D. Frequency is 200Hz, Fig3E.Frequency is 250Hz, Fig3F. Frequency is 300Hz
Fig3G. Frequency is 400Hz, Fig3H. Frequency is 450Hz, Fig3I. Frequency is 500Hz

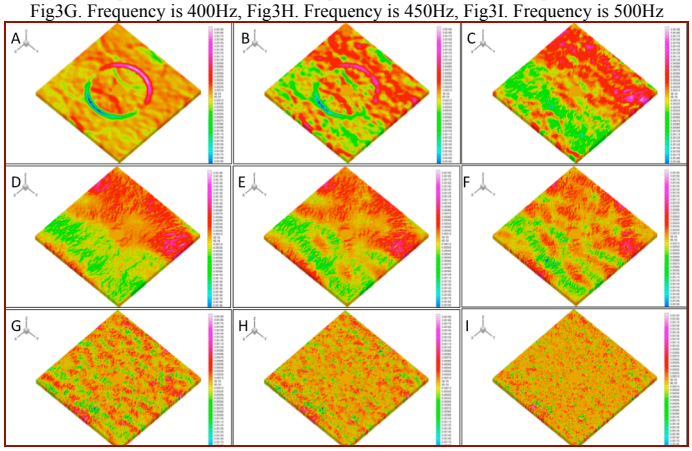

Figure 4. Dynamic stress in x direction as function of frequency at undrained state under earthquake wave
Fig4A. Frequency is 10Hz, Fig4B. Frequency is 50Hz, Fig4C. Frequency is 100Hz
Fig4D. Frequency is 200Hz, Fig4E. Frequency is 250Hz, Fig4F. Frequency is 300Hz
Fig4G. Frequency is 400Hz, Fig4H. Frequency is 450Hz, Fig4I. Frequency is 500Hz

The dynamic stress in x and y direction as function of frequency at undrained state are shown in the Fig.4 and Fig.5, the low frequency dynamic stress destroy the structure closed to the surface of the pore-network cracks, the high frequency dynamic stress destroy the structure far from the pore-network cracks surface. The low frequency earthquake wave have little energy than frequency part, with the distance (far from the front of the crack) increased, their effect to the structure of the tight sandstone decreased sharply; while the high frequency carry major energy of the earthquake wave, their effect distance to the tight sandstone can reach the whole zone. All these results are consisted with the observation data in tight sandstone liquefaction process in nature earthquake[25-28].

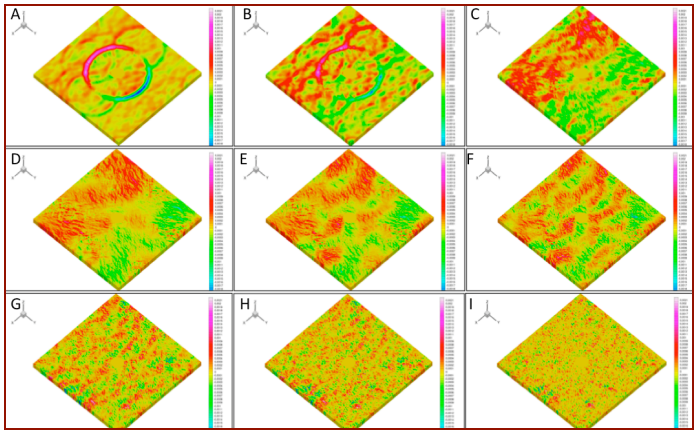

Figure 5. Dynamic stress in y direction as function of frequency at undrained state under earthquake wave

Fig5A. Frequency is 10Hz, Fig5B. Frequency is 50Hz, Fig5C. Frequency is 100Hz
Fig5D. Frequency is 200Hz, Fig5E. Frequency is 250Hz, Fig5F. Frequency is 300Hz
Fig5G. Frequency is 400Hz, Fig5H. Frequency is 450Hz, Fig5I. Frequency is 500Hz

The transient liquefaction process as function of frequency of the earthquake wave are plotted in Fig.6, when the frequency of the earthquake is higher than 1250Hz, the electromagnetic wave energy make the fluid volume in the three-dimensional pore-network cracks changed sharply, let the dynamic stress in the three-dimensional pore-network cracks surface (solid sketch interface) exceed the solid sketch part strength criteria in 10E-5s, the liquefaction in the micro tight sandstone zone appears in 10E-5s and propagates to the whole domain zone of the tight sandstone in 10E-5s, only seldom higher strength components in the tight sandstone can keep macro-structure (the white zone in the Fig 6D).

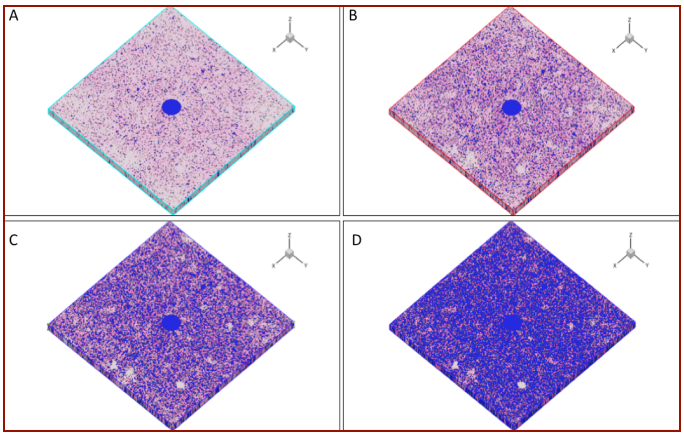

Fig 6. The transient liquefaction process as function of frequency of the earthquake wave
Fig6A. Frequency is 500Hz, Fig6B Frequency is 750Hz, Fig6C. Frequency is 1000Hz, Fig6D Frequency is 1250Hz

5.2 Hydrofacturing-liquefaction process varying with the amplitude of earthquake wave

The pore-network cracks hydrofacturing-liquefaction process as function of the amplitude of the earthquake wave is shown in the Fig. 7, at the fixed constituting time and frequency of the earthquake condition, when the amplitude is arrange at 0.01GPa~0.03GPa, the surface of the pore-network cracks begin propagate, the hydrofracturing around the big pore-network cracks fronts appear, and the liquefaction phenomena do not happen; with the amplitude of the earthquake increased, when it reach to 0.05GPa~0.07GPa, the coupled hydrofacturing-liquefaction begin at most of the pore-network cracks fronts; when the amplitude of the earthquake is exceeded to 0.07GPa~0.1GPa, the pore-network cracks propagate sharply and the hydrofacturing-liquefaction happen in the whole tight sandstone zone, only seldom components micro structure do not failure(white zone in Fig7E, 7F).

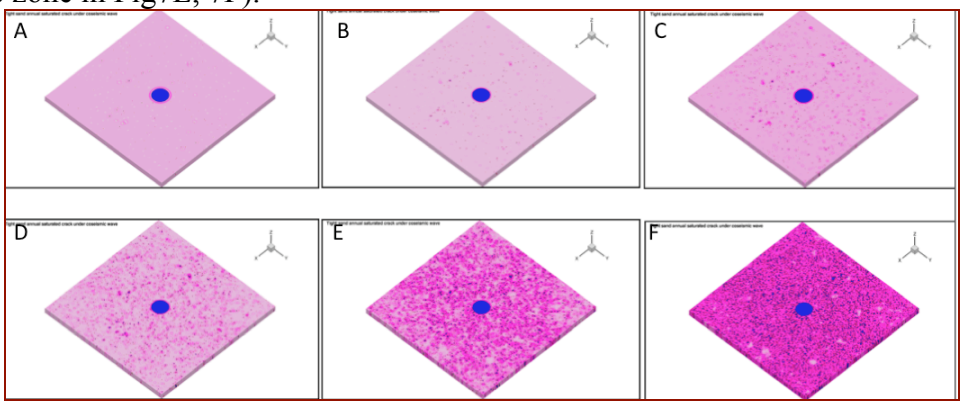

Fig 7. The cracking propagating process variation as the AM of the earthquake wave
Fig7A. AM of earthquake wave is 0.01GPa, Fig7B AM of earthquake wave is 0.03GPa, Fig7C AM of earthquake wave is 0.05GPa
Fig7D. AM of earthquake wave is 0.07GPa, Fig7E AM of earthquake wave is 0.09GPa, Fig7F AM of earthquake wave is 0.1GPa

The distribution of dynamic stress in x and y direction as function of amplitude of the earthquake are shown in the Fig.8 and Fig 9, respectively. When the amplitude arrange at 0.01GPa~0.03GPa, the electromagnetic wave and stress wave propagation far in the tight sandstone, for the whole tight

sandstone structure remains intact, low earthquake energy consumed in the spreading process; When the amplitude of the earthquake reach to 0.05GPa~0.07GPa, with the pore-network cracks propagation, the non-connected pore throats in the tight sandstone are destroyed quickly, most of the earthquake energy are used to providing the surface energy of the pore-network cracks interface, the electromagnetic wave and stress wave propagation distance decrease with the amplitude increasing; When the amplitude of the earthquake is exceeded to 0.07GPa~0.1GPa, the vase majority non-connected pore throats in the tight sandstones are destroyed and the whole tight sandstone structure instability and failure, the propagation media of the electromagnetic wave and stress wave translate from solid (tight porous structure) to fluid (liquefaction sandstone structure), their spreading distance decreased sharply.

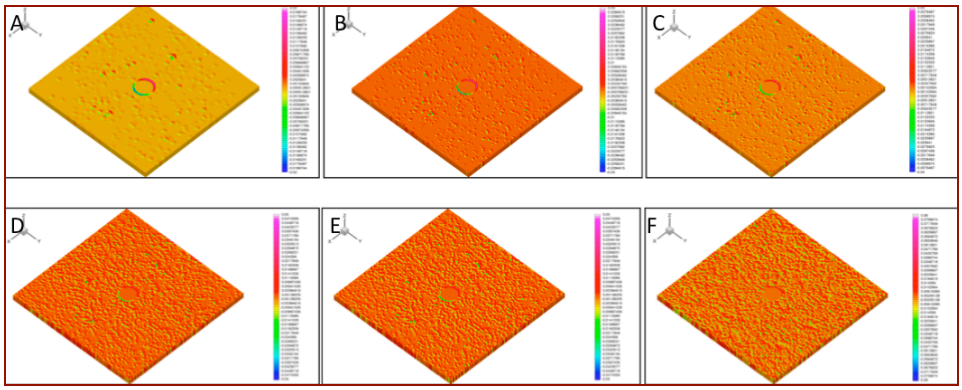

Figure 8. Dynamic stress in x direction variation as function of time at undrained state under earthquake
Fig8A. AM of earthquake wave is 0.01GPa, Fig8B AM of earthquake wave is 0.03GPa, Fig8C AM of earthquake wave is 0.05GPa
Fig8D. AM of earthquake wave is 0.07GPa, Fig8E AM of earthquake wave is 0.09GPa, Fig8F AM of earthquake wave is 0.1GPa

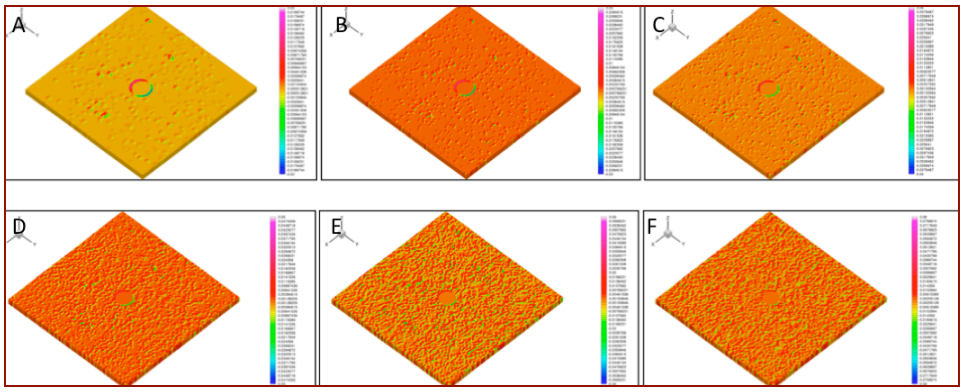

Figure 9. Dynamic stress in y direction variation as function of time at undrained state under earthquake wave
Fig9A. AM of earthquake wave is 0.01GPa, Fig9B AM of earthquake wave is 0.03GPa, Fig9C AM of earthquake wave is 0.05GPa
Fig9D. AM of earthquake wave is 0.07GPa, Fig9E AM of earthquake wave is 0.09GPa, Fig9F AM of earthquake wave is 0.1GPa

In general, both high frequency and amplitude of the earthquake wave are the main factors which lead to the pore-network cracks transient Hydrofracturing-liquefaction process; high frequency of electromagnetic wave and stress wave make the porous and permeability of the tight sandstone changed sharply in 10E-5s which lead the strength criteria of the tight sand stone decrease; high amplitude of the electromagnetic wave and stress wave make the dynamic pore stress in the tight sandstone changed sharply in 10E-5s which lead the maximum principle stress increased to the macro tight sandstone strength criteria; all these leading to pore-network cracks propagation, local area hydrofacturing-liquefaction, and the eventual entire region liquefaction occurred. All these results are consisted with the nature earthquake liquefaction observation data [28, 29].

At practice drilling project, with the hydro-pressure increasing, the pore stress in the tight sandstone is reach to the maximum principal stresses and the sandstone begin failure, this stage is a static/quasi-static process which including the drained propagation; once the tight sandstone begin rupture, this means that the micro pore-network cracks begin propagation, the pore stress will spreading as stress wave way, the stage is transient process and the drained propagation do not happen. The results well consisted with the practical observation data and can well explain why

secondary hydrofacturing stage maximum principal stress reduced.

6. Conclusions

In this work, an novel intricate theoretical analysis and numerical simulations methods (LB-FE-HIE) is proposed by the author to explore the three-dimensional pore-network cracks transient hydrofacturing-liquefaction in tight sandstone under seismic wave & electro-magneto-thermo-elastic field. The conclusion can be drawn as follows.

1. The problem is reduced to solving a set of coupled lattice Boltzmann & finite element & hypersingular integral equations by using the Green functions and distribution functions.

2. The behavior of the extended displacement discontinuities around the pore-network cracks surface terminating at the solid-liquid film interface is analyzed. Analytical solutions for the extended singular dynamic stresses, the extended dynamic stress intensity factors and the extended dynamic energy release rate near the dislocations front are provided.

3.The tight sandstone sample from the Ordos Basin Triassic formation is selected and the fluid-solid coupled digital rock physical modeling is established. The simulations of 3D PC-TH-TS process is presented, the hydrofacturing-liquefaction varying with the amplitude, frequency and time of earthquake wave is obtained, the results are consisted with the nauture earthquake observation data and practical drilling project observation data.

4. The relationship between the tight sandstone pore-network cracks transient propagation-evolution and the maximum tight sandstone fracturing-liquefaction stress criteria is explored, which are useful to guide the in-situ stress measurement in practical drilling project and are helpful to understand the liquefaction mechanismu of earthquake.

Acknowledgements

The work was supported by National Natural Science Foundation of China (NOD0408/4097409), Chairmen Foundation of UCAS [A](D0408/4097409) and Deep exploration in China-Sinoprobe-04 (0819011A90).

References

[1] Fan TY. Propagating Semi-Infinite Crack in Fluid-Saturated Porous-Medium of Finite Height. Theor Appl Fract Mec 1991;16:237.

[2] Kachanov M, Tsukrov I, Shafiro B. Materials with fluid-saturated cracks and cavities: Fluid pressure polarization and effective elastic response. Int J Fracture 1995;73:R61.

[3] Loret B, Radi E. The effects of inertia on crack growth in poroelastic fluid-saturated media. J Mech Phys Solids 2001;49:995.

[4] Cheng CM, Tan QM, Peng FJ. On the mechanism of the formation of horizontal cracks in a vertical column of saturated sand. Acta Mech Sinica 2001;17:1.

[5] Galvin RJ, Gurevich B. Interaction of an elastic wave with a circular crack in a fluid-saturated porous medium. Appl Phys Lett 2006;88.

[6] Lu XB, Zheng ZM, Wu YR. Formation mechanism of cracks in saturated sand. Acta Mech Sinica 2006;22:377.

[7] de Borst R, Rethore J, Abellan MA. A numerical approach for arbitrary cracks in a fluid-saturated medium. Arch Appl Mech 2006;75:595.

[8] Galvin RJ, Gurevich B. Scattering of a longitudinal wave by a circular crack in a fluid-saturated

porous medium. Int J Solids Struct 2007;44:7389.
[9] Barani OR, Khoei AR, Mofid M. Modeling of cohesive crack growth in partially saturated porous media; a study on the permeability of cohesive fracture. Int J Fracture 2011;167:15.
[10] Wang XQ, Schubnel A, Fortin J, David EC, Gueguen Y, Ge HK. High Vp/Vs ratio: Saturated cracks or anisotropy effects? Geophys Res Lett 2012;39.
[11] Sarout J. Impact of pore space topology on permeability, cut-off frequencies and validity of wave propagation theories. Geophys J Int 2012;189:481.
[12] B.J.Zhu, C.Liu, Y.L.Shi, X.Y.Liu. Saturated dislocations transient propagation–evolution in olivine structure under ultra high-coupled thermal-force fields. Theor Appl Fract Mec 2012;58:9.
[13] Zhu BJ, Qin TY. Hypersingular integral equation method for a three-dimensional crack in anisotropic electro-magneto-elastic bimaterials. Theoretical and Applied Fracture Mechanics 2007;47:219.
[14] Bojing Z, Taiyan Q. Application of hypersingular integral equation method to three-dimensional crack in electromagnetothermoelastic multiphase composites. Int J Solids Struct 2007;In Press, Accepted Manuscript.
[15] Aboudi J. Micromechanical analysis of fully coupled electro-magneto-thermo-elastic multiphase composites. Smart Materials & Structures 2001;10:867.
[16] Perez-Aparicio JL, Sosa H. A continuum three-dimensional, fully coupled, dynamic, non-linear finite element formulation for magnetostrictive materials. Smart Materials & Structures 2004;13:493.
[17] H.H.Cheng, Y.C.Qiao, C.Liu, Y.B.Li, B.J.Zhu, Y.L.Shi, D.S.Sun, K.Zhang, W.R.Lin. Extended hybrid pressure and velocity boundary conditions for D3Q27 lattice Boltzmann model. Applied Mathematical Modelling 2012;36:2031.
[18] Ma J, Wu K, Jiang Z, Couples GD. An implementation for lattice Boltzmann simulation in low-porosity porous media. Phys Rev A 2010;E 81, 056702.
[19] Jiang Z, Wu K, Couples G. The Impact of Pore Size and Pore Connectivity on Single-Phase Fluid Flow in Porous Media. Advanced Engineering Materials. 2010;doi: 10.1002/adem.201000255.
[20] Zhu B, Cheng H, Qiao Y, Liu C, Shi Y, Zhang K, Sun D, Lin W. Porosity and permeability evolution and evaluation in anisotropic porosity multiscale-multiphase-multicomponent structure. Chinese Sci Bull 2012;57:320~327.
[21] Dmitriev NM. Surface porosity and permeability of porous media with a periodic microstructure. fluid Dynamics 1995;30:64~69.
[22] C.Y K, J.D F, J.L.A C. Image analysis determination of stereology based fabric tensors. Geotechnique 1998 48:515~525.
[23] Koo J, Kleinstreuer C. Liquid flow in microchannels: experimental observations and computational analyses of microfluidics effects. JOURNAL OF MICROMECHANICS AND MICROENGINEERING 2003:568~579.
[24] Qin TY, Tang RJ. Finite-Part Integral and Boundary-Element Method to Solve Embedded Planar Crack Problems. Int J Fracture 1993;60:373.
[25] Wang CY. Liquefaction beyond the near field. Seism. Res. Lett. 2007;78:512.
[26] Popescu R. Finite element assessment of the effects of seismic loading rate on soil liquefaction. Canadian Geotech. J 2002;29:331.

[27] Ghosh B, Madabhushi SPG. A numerical investigation into effects of single and multiple frequency earthquake motions. Soil Dynamics and Earthquake Engineering 2003;23:691－704.
[28] Kilb.D., J.Gomberg, P.Bodin. Aftershock triggerinig by complete Coulomb stress changes. J.Geophys.Re 2002;107:doi:10.1029/2001JB000202.
[29] Ishihara K. Soil Behavior in Earthquake Geotechnics,. Oxford: Clarendon Press. 1996:350.